Diffuse X-ray Emission from M101
September 19, 2002

K. D. KUNTZ[1]

Department of Physics, University of Maryland Baltimore County
1000 Hilltop Circle, Baltimore MD, 21250
kuntz@milkyway.gsfc.nasa.gov

S. L. SNOWDEN[2], W.D. PENCE, and K. MUKAI[2]

Laboratory for High Energy Astrophysics
Code 662, NASA/GSFC, Greenbelt, MD 20771
snowden@riva.gsfc.nasa.gov
pence@tetra.gsfc.nasa.gov
mukai@milkyway.gsfc.nasa.gov

ABSTRACT

The total 0.45-2.0 keV luminosity of M101 is 3.1×10^{39} ergs s^{-1}, of which 2.2×10^{39} ergs s^{-1} is due to diffuse emission. Of the diffuse emission, no more than 6% can be due to unresolved point sources such as X-ray binaries, and $\sim 11\%$ is due to dwarf stars. The diffuse emission traces the spiral arms and is roughly correlated with the Hα and FUV emission. The radial distribution closely follows the optical profile. The bulk of the diffuse emission is characterized by a two-thermal-component spectrum with $kT = 0.20, 0.75$ keV, and the ratios of the emission measures of the two components is roughly constant as a function of both radius and surface brightness. The softer component has a sufficiently large covering factor that the bulk of the emission is likely extra-planar. We find no evidence of an extended axisymmetric X-ray halo, suggesting that any such halo has a strength much smaller than current predictions.

Subject headings: X-rays-diffuse background — X-rays:ISM

1. Introduction

M101 (NGC 5457) is a nearby face-on spiral galaxy that lies in a direction of low Galactic absorption. As such, it is an ideal target for the study of the hot component of the ISM in a "typical" spiral galaxy, allowing high spatial resolution at relatively soft energies.

---

[1] Mailing address: Laboratory for High Energy Astrophysics, Code 662, NASA/GSFC, Greenbelt, MD 20771

[2] Universities Space Research Association

1.1. Previous Results

Previous studies of the diffuse emission from M101 have been executed with *Einstein* (McCammon & Sanders 1984; Trinchieri et al. 1990), *ROSAT* PSPC (Snowden & Pietsch 1995; Wang et al. 1999), *ROSAT* HRI (Wang et al. 1999), and ASCA (Wang et al. 1999). These studies are characterized by relatively poor spatial resolution that hindered point source detection and placed large uncertainties on the amount of diffuse emission.

The PSPC study demonstrated the existence of diffuse $\frac{1}{4}$ keV emission with a filling factor of ~ 1 and a color temperature of $10^{5.8}$ K ($kT = 0.054$ keV) The temperature and large filling factor

prompted the authors to suggest that the $\frac{1}{4}$ keV emission was primarily in the halo; if the emission were from the disk and due to regions like the Local Hot Bubble (Snowden et al. 1998), with a typical overburden of a few times 10^{20} cm^{-2}, the filling fraction would be significantly more than unity, and the temperature would be much smaller than that observed for hot Galactic bubbles. Given a resolution of $\sim 1'$, a primary concern was the contribution to the diffuse emission by unresolved point sources. Arguments were made that there was no known population of sources that could produce the amount of $\frac{1}{4}$ keV emission seen.

A PSPC study of the $\frac{3}{4}$ keV band (R45, 0.44-1.21 keV) is more comparable to the present *Chandra* study. Snowden & Pietsch (1995) determined an R45 band color temperature of $10^{6.53}$K ($kT = 0.29$ keV), a flux within the inner $7'\!.5$ of 5.8×10^{-13} ergs cm^{-2} s^{-1}, and a luminosity of 3.6×10^{39} ergs s^{-1}. Again there was a concern about the contributions from unresolved point sources, but there were insufficient source statistics to attempt a correction. Contributions from sources such as M dwarfs could be reasonably well constrained and shown to be small.

Wang et al. (1999) also came to the conclusion that no known population of sources could explain the entire emission seen in the central region of M101. They further attempted to constrain the temperature of the diffuse emission in the central $5'$ with a joint fit to the *ROSAT* PSPC and *ASCA* GIS spectra. Given the angular resolution of the PSPC, and the poorer angular resolution of the GIS, they did not attempt to remove the point sources, but attempted to compensate by modeling the aggregate spectrum of the point sources. Modeling the point sources with either thermal or power law spectra produced a diffuse component with $kT = 0.186$ keV (T=$10^{6.335}$).

1.2. Aim of the Present Work

The angular resolution of *Chandra* not only allows point source detection and removal to unprecedented levels, but also allows the construction of the point source luminosity function, the extrapolation of which places strict upper limits on the possible contribution of unresolved sources to the diffuse emission. The catalogue of point sources and the luminosity function were presented in Pence et al. (2001), while discussion of

some individual objects is contained in Snowden et al. (2001) and Mukai et al. (2002). The purpose of the present work is to determine the distribution, luminosity, and gross spectral characteristics of the soft diffuse X-ray emission from M101.

Due to the electronic noise feature, the *Chandra* energy interval is approximately $E > 0.45$ keV. In this energy interval the disk of M101 ranges from nearly transparent at all energies to, at worst, $\tau \sim 2.7$ at 0.45 keV. As M101 is nearly face on, we are "X-raying" the entire disk, detecting most of the gas hot enough to produce significant emission above 500 eV. The observed emission will contain contributions from HII regions, SNR, hot bubbles, and galactic chimneys, but the faintness of each individual object, or the lack of contrast from neighboring emission regions, restrict the spectral analysis to the bulk properties of the hot gas.

2. Data

The data analyzed here are derived from a single 98.2 ks *Chandra* exposure taken in AO1 using the ACIS-S3 back-side illuminated chip. The aimpoint was placed near the nucleus and the roll-angle adjusted so that the bulk of the $\frac{1}{4}$ keV emission detected by *ROSAT*, as well as the giant H II regions NGC 5461 and NGC 5462, would fall on the S3 chip. The configuration was also chosen to maximize the radial extent over which we could study the emission, as well as to leave space for "blank" sky from which to determine the background. Other chips were on during the exposure but, due to their distance from the aim-point or poorer low-energy response, are of little use for this analysis. The most recent gain files were used; response and redistribution functions were extracted from the CIAO Caldb 2.12.

The light-curve was constructed for the entire chip in the 2.0-7.0 keV band to allow the detection and removal of background flares. Three minor flares were detected and discarded, reducing the exposure to 92.3 ks. There are often low-level flares that are undetectable from the light-curve, but which produce a significant spectral signature in the 2.0-7.0 keV band. The contribution from these flares is discussed in §3.1.1.

2.1. Point Source Removal

Although the bulk of the diffuse emission emits at energies less than ~ 1500 eV, in order to produce the cleanest spectrum of the diffuse emission, we removed sources detected to 3.5 σ in any of a series of energy bands covering the the entire *Chandra* energy range. Point sources were detected using the *wavdetect* routine in the 350-1300 eV, 500-2000 eV, and 2000-8000 eV bands. (All of the sub-bands used in Pence et al. (2001) were processed in a similar way, but did not produce significant sources that were not found in three bands listed here.) Significance was determined using Poisson statistics; the source counts being determined from an elliptical 75% encircled energy region with the same aspect ratio and orientation as the PSF, and the background counts being determined from a concentric elliptical annulus extending from 2 to 3 times the 95% encircled energy radius. A larger region was removed from around source P98 (Pence et al. 2001) due to its extreme brightness.

The log N-log S relation in the 0.5-2.0 keV energy interval is shown in Pence et al. (2001) and extends to luminosities $\sim 10^{36}$ erg s^{-1}. Extrapolating the log N-log S to lower luminosities is not trivial due to rapid changes in the source population with luminosity. In the Galaxy, the Low-Mass X-ray Binary (LMXB) population dominates for 10^{36} erg s^{-1} $< L < 10^{38}$ erg s^{-1}, but tails off sharply below 10^{36} erg s^{-1}. High-Mass X-ray Binaries (HMXB) with evolved companions have luminosities 10^{35} erg s^{-1} $< L < 10^{37}$ erg s^{-1}, but only half the spatial density of persistent LMXBs. Below 10^{35} erg s^{-1}, a number of other populations exist, such as persistent Be X-ray binaries, whose density with respect to that of LMXBs is poorly understood. Assuming a source spectrum with $\Gamma = 2$ and directly extrapolating the Pence et al. (2001) log N-log S relation to luminosities 10^{35} and 10^{34} erg s^{-1} produces 4.1% and 5.8% of the observed diffuse emission.

3. Large-Scale Diffuse Emission

3.1. Morphology & Photometry

Figure 1 displays the chip S3 data after point source removal and smoothing by a 7″.9 FWHM Gaussian. The lower parts of Figure 1 contain the
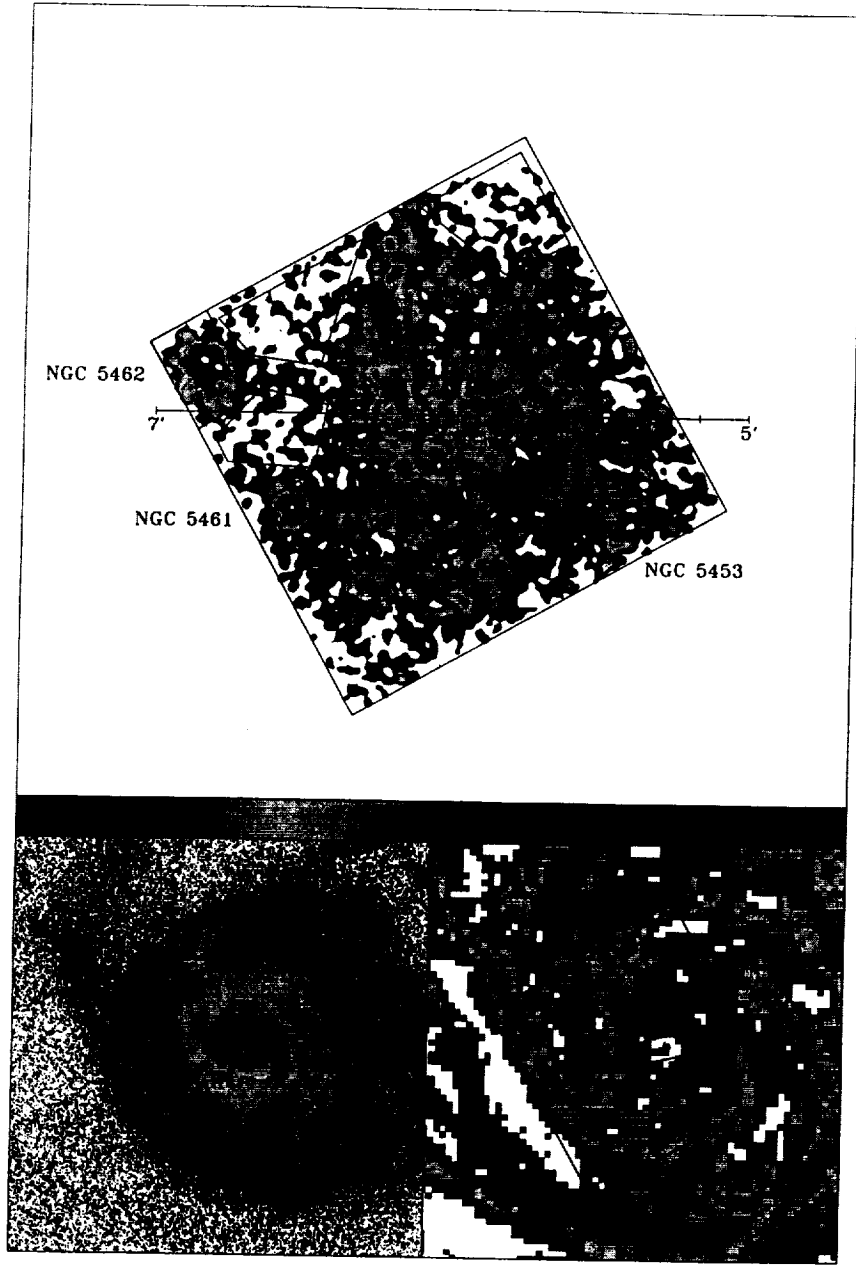
Fig. 1.— *Top:* The X-ray image in the 0.45-1.0 keV interval after point source removal, smoothed by a Gaussian with a HWHM of $3''94$ (8 pixels). The color intervals are 1.6×10^{-6} counts cm^{-2} s^{-1} $arcmin^{-2}$, starting at the value of the background. White regions surrounded by high surface brightness regions denote the removal of point sources with large PSFs. The irregular polygons are the regions used to determine the background. The rule is marked in arcminutes from the nucleus. *Bottom Left:* Optical image from the Palomar Sky Survey, with the position of the S3 chip marked. The ellipse marks the size and position of the large-scale CO bar. *Bottom Right:* HI 21 cm image. The color scales runs from 10^{20} cm^{-2} (white) to 2×10^{21} cm^{-2}.

4

optical and HI 21 cm images. It is immediately apparent that the X-ray emission is strongly correlated with the spiral arms, and that a significant fraction of the X-ray emission is due to the giant HII regions NGC 5461 and NGC 5462. The nuclear emission is, in fact, smaller than the emission in either of the giant HII regions. Many, but not all, of the knots of X-ray emission are correlated with HII regions (see Figure 2), and the stronger knots have associated "point sources" which may be, alternatively, compact diffuse emission regions or compact clusters of X-ray sources. The correlation of X-ray emission with the HI holes is as poor as the correlation between HI holes and Hα emission noted by Kamphuis (1993). (Since the lifetime over which an HI hole can be observed is $\sim 5 \times 10^7$ years, and the generating HII regions last $\sim 2 \times 10^7$ years, Kamphuis argued that two-fifths of the holes should contain HII regions. In our sample, there are thirteen large HI holes; three are clearly filled with emission stronger than that of the surrounding disk, another three have X-ray emission comparable to the surrounding disk, and seven have less X-ray emission than the surrounding disk. The HI holes that are filled by X-ray emission tend to have HII regions that are not near the peak of the X-ray emission, while X-ray empty HI holes tend to have X-ray emission and correlated HII regions on their edges.)

We have compared the *Chandra* image with a FUV (1521Å) image from the *Ultraviolet Imaging Telescope (UIT)* (Stecher et al. 1997). As can be seen in Figure ??, the regions of diffuse X-ray emission are in general well correlated with the regions of diffuse UV emission. Most knots of X-ray emission are correlated with knots of UV emission, though there are some notable exceptions particularly the diffuse emission around P98, which may in fact be due to the wings of the PSF, and the arc-like emission region north-east of the nucleus. A number of the more intense FUV emission knots are not associated with peaks in the X-ray emission. Some of these knots of FUV emission are on the *edges* of knots of X-ray emission, perhaps suggesting the propagation of star formation; the knot of X-ray emission being associated with SNR or an aggregation of young X-ray binaries, while the adjacent FUV emission region is associated with young high-mass stars.

3.1.1. Determining the Background

We had placed the nucleus near the aim-point of the S3 chip and specified a roll angle so that the bulk of the *ROSAT* $\frac{1}{4}$ keV emission would fill the S3 chip. The expectation was that the diffuse emission detected by *Chandra*, being significantly harder would, like the *ROSAT* $\frac{3}{4}$ keV emission, cover a significantly smaller area, and that the corners would be relatively free of contamination by M101. Instead, we found that *Chandra's* greater sensitivity allows one to trace that emission at least to the edge of the chip in almost every direction.

In Figure 1 the three irregular polygons indicate regions with "low" surface brightness between strong spiral arms. The three regions contain statistically identical spectra. The mean spectrum from these regions, after the removal of the instrumental background (§3.2) is shown in Figure 3. There is significant flux in the 2-5 keV interval essentially all of which is due to the particle background from unremoved low-level flares. By comparing the background spectrum in the observation of GK Per in periods with and without flares, one can show that the particle background during flares has a power law shape, without convolution with the response function. We have assumed that the spectral shape of low-level flares is similar to that of the stronger flares. To remove the residual low-level flares from the M101 observation, the 2-5 keV interval was fit with an unconvolved power law, and those parameters transferred to the fits in the 0.45-2.0 keV interval.

The dashed line in Figure 3 is a model for the Galactic foreground/extragalactic background calculated for a 5°×5° box in the direction of M101 from the *ROSAT* All-Sky Survey (RASS) using the method of Kuntz & Snowden (2000). The extragalactic background (dotted line) is modeled by a power law of index 1.46 and a normalization of 10.5 keV cm^{-2} s^{-1} sr^{-1} keV^{-1} (Chen et al. 1997). From the extragalactic background was removed the flux due to resoved point sources, as modeled by Mushotzky et al. (2000). The extragalactic emission was then absorbed by the disk of M101 ($\sim 4.4 \times 10^{20}$ cm^{-2}). The Galactic foreground model contains contributions from the Local Hot Bubble (unabsorbed) and a two thermal-component Galactic halo absorbed by 9×10^{19}
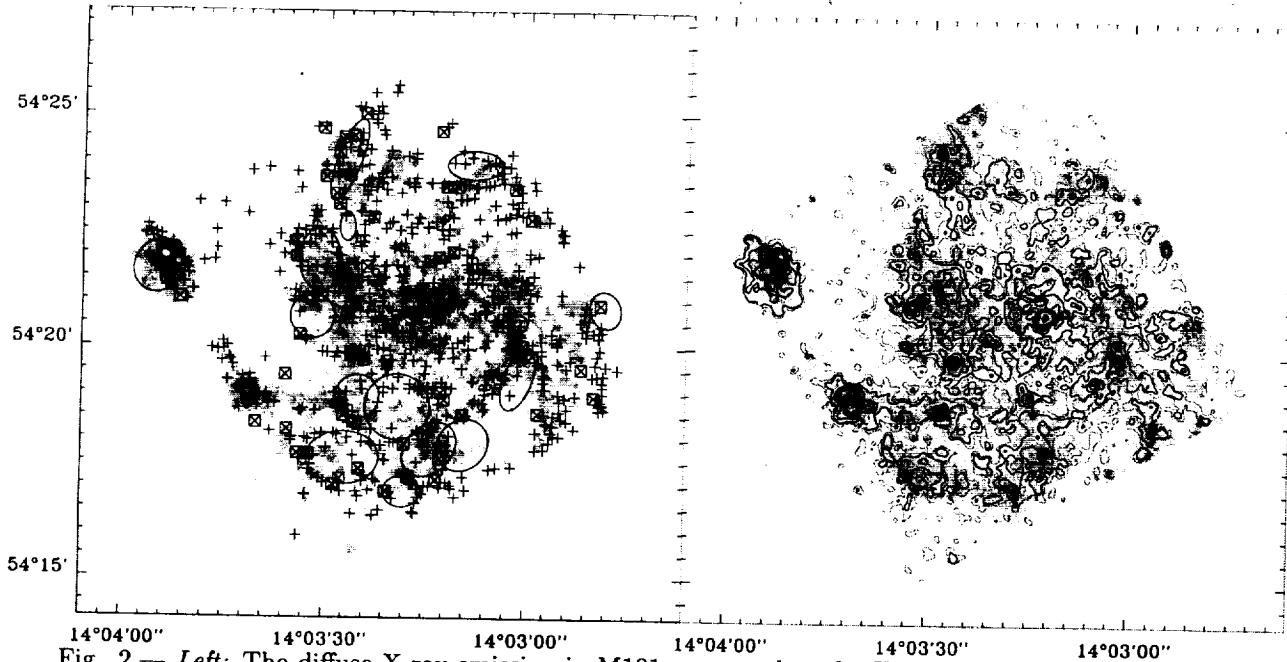
Fig. 2.— *Left:* The diffuse X-ray emission in M101 compared to the HII regions from Hodge et al. (1990) (crosses), the HI holes listed by Kamphuis (1993) (ellipses), and the supernova remnants of Matonick & Fesen (1997) (boxes). *Right:* The UIT image (greyscale) compared to the X-ray image (contours).
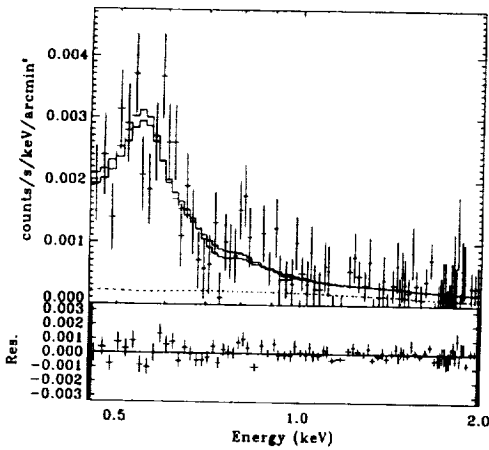

Fig. 3.— Spectrum in the background regions. The best *ROSAT* model and the best fit *Chandra* spectrum are shown by the solid line. The dotted line is contribution by the unresolved background sources.

cm^{-2}. Since the Raymond & Smith model temperature for the Local Hot Bubble is well constrained by a series of *ROSAT* observations (Snowden et al. 1998; Kuntz & Snowden 2000; Snowden et al. 2000), that parameter was fixed to $T=10^{6.11}$ in the *RASS* fits, but all the other parameters were allowed to vary. The solid line is the best fit of this model to the *Chandra* data for the low surface brightness regions.

It is not known whether the harder Galactic halo component is truly Galactic, or whether it may be in part extragalactic. Assuming it is extragalactic and absorbed by the M101 disk reduces the transmitted flux by only 4%.

The relevant point is that the *ROSAT* model for the Galactic foregrounds in the direction of M101 produces a spectrum similar to that seen in between the arms of M101, with nearly the same normalization. The best fit model to the Chandra data produces 77.8×10^{-6} counts s^{-1} arcmin^{-2} in *ROSAT* band R45, while the *ROSAT* All-Sky Survey contains $(81.8 \pm 4.2) \times 10^{-6}$ counts s^{-1} arcmin^{-2} for a square degree surrounding but not including M101. Thus, the low-surface-brightness interarm regions from which these spectra were
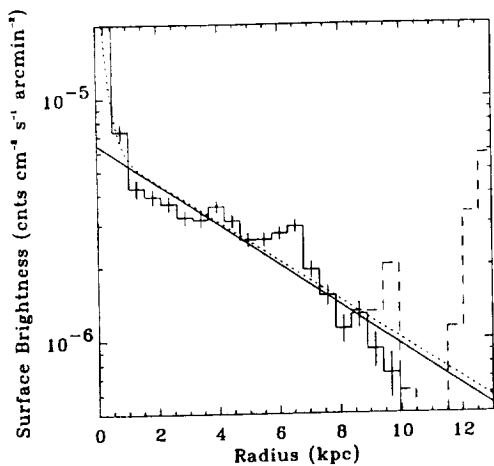
6

Fig. 4.— The 0.45-1.0 keV X-ray surface brightness as a function of radius. The solid histogram excludes the giant HII regions; the dashed histogram includes the giant HII regions. The solid line is the fitted exponential. The dotted line is the optical profile from Okamura et al. (1976) scaled to the same central surface brightness for the exponential disk.

derived appear to have very little contamination by emission from M101 itself. We have used this spectrum as the Galactic foreground spectrum.

3.1.2. Surface Brightness and Total Flux

The radial profile of the 0.45-1.0 keV emission is shown in Figure 4. As might be expected, the two giant HII regions produce large perturbations to the radial distribution. Without the contribution of the giant HII regions, the X-ray exponential scale length is 5.24 ± 0.49 kpc, similar to the scale lengths in both the V band, $R_V = 5.19$ kpc, and the B band, $R_B = 5.40$ kpc (Okamura et al. 1976).

Excluding the giant HII regions, the total flux within a radius of 10 kpc is 1.5×10^{-4} counts cm^{-2} s^{-1} in 0.45-1.0 keV. The giant HII regions provide an additional 0.24×10^{-4} counts cm^{-2} s^{-1} in 0.45-1.0 keV. Since the flux is dominated by the low-surface-brightness regions we used the spectrum of the low surface brightness gas to find a conversion to physical units of 1.60×10^{-9} ergs count^{-1}, and thus a total 0.45-1.0 keV luminosity of 1.77×10^{39} ergs s^{-1}, or a 0.5-2.0 keV flux of 2.05×10^{39} ergs s^{-1}. Within a radius of 10 kpc, the total luminos-

ity of point sources (other than P98) is 0.82×10^{39} ergs s^{-1}. Extrapolating the exponential relation shown in Figure 4, assuming a $\Gamma = 2.0$ spectrum for the point sources, and adding the flux due to the nuclear region and the giant HII regions, we find a luminosity of 3.86×10^{39} ergs s^{-1} in the central 7.5 in the 0.45-1.0 keV interval. This value compares well to the 3.6×10^{39} ergs s^{-1} found by ROSAT in the same region in the 0.44-1.21 keV interval (Snowden & Pietsch 1995), further implying that about 45% of the "diffuse" ROSAT flux was due to unresolved point sources.

3.1.3. Color Gradients

A brief glance at the spectra in following sections reveals that the emission in the 0.45-2.0 keV interval is dominated by OVII (0.560 keV), OVIII (0.650 keV), and a complex of iron lines in the .7-1.0 keV interval. For a first-order understanding of the diffuse emission we considered the (.70-1.0)/(.45-.70) hardness ratio. Because the count rate is low, and thus the counting statistics poor, we present the hardness ratio as functions of radius and of surface brightness (Figure 5) rather than as a map. The hardness ratio is constant at low surface brightnesses (below $\sim 10^{-5}$ counts cm^{-2} s^{-1} arcmin^{-2}). In the surface brightness interval $(1.3-1.8) \times 10^{-5}$ counts cm^{-2} s^{-1} arcmin^{-2} the hardness ratio is much higher. However, the bulk of this emission comes from a limited number of compact, bright emission regions, some of which are identified as HII regions (Hodge et al. 1990). Above 2×10^{-5} counts cm^{-2} s^{-1} arcmin^{-2}, the emission comes from the nucleus and the giant HII regions. There is a slight and statistically insignificant increase of hardness with surface brightness for the nucleus, and a greater increase (though still statistically insignificant) for the giant HII regions. There is no statistically significant trend of hardness with radius.

3.2. Spectroscopy

The background spectrum is a combination of the Galactic foregrounds, the extragalactic background, and the instrumentation particle background. The particle background spectrum was derived from the "dark moon" data and scaled to this observation/region using the particle background rate in the 10.5-14.5 keV region, where Chandra has an insignificant response to cosmic

Fig. 6.— A raw spectrum of the diffuse emission. The lower spectrum is the background. Features at 1.2 and 1.38 keV (see §3.2) are apparent in the raw spectrum; the 1.2 keV feature may have been augmented by the background subtraction.
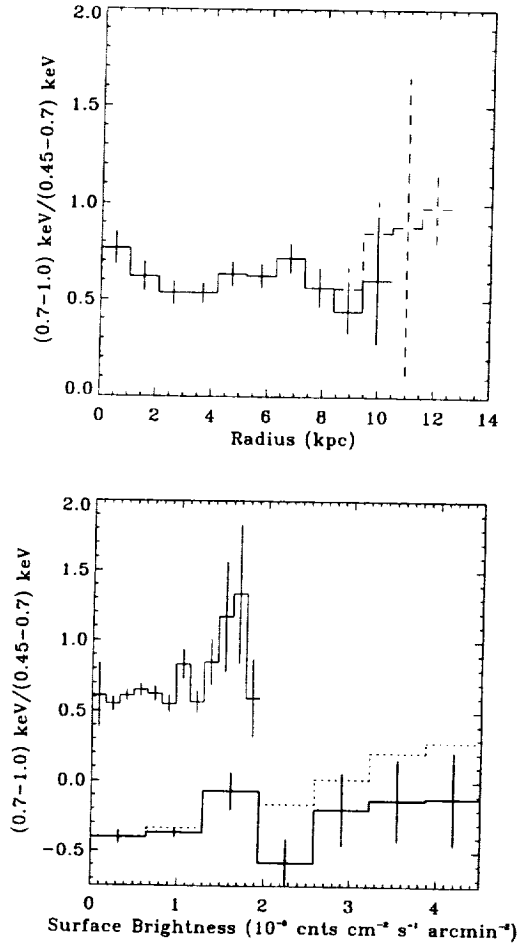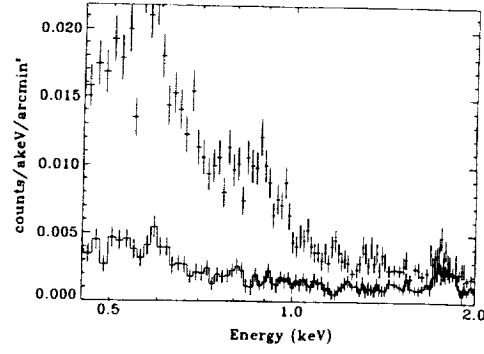
Fig. 5.— *Top:* The hardness ratio as a function of radius. The solid line excludes the giant HII regions; the dashed line includes the giant HII regions. *Bottom:* The hardness ratio as a function of surface brightness. The lower histogram is more broadly binned, and is offset in color by -1. The upper histogram above 1.3×10^{-6} counts cm^{-2} s^{-1} $arcmin^{-2}$ is dominated by a small number of bright knots.

X-rays. The Galactic foreground/extragalactic background spectrum was derived from the background regions noted in §3.1.1. The ratio of the response in the region covered by M101's diffuse emission to the response in the background region is energy dependent, and can vary from one to five percent over a hundred eV. Since the particle background is patterned (Markevitch 2001)

the particle background spectrum will not scale with area. Therefore, we removed the appropriate particle background spectrum from the spectrum extracted from the background regions, scaled the result by the ratios of the reponses and areas, and added the correct particle background spectrum for the diffuse emission, propagating all uncertainties. Figure 6 shows a raw spectrum of the large-scale diffuse emission and its background, as computed by the method outlined above.

Since the exposure was made on day 247 after launch, the accumulating absorption thought to be due to organics condensing on either the chips or the filters is negligible.

We have used solar metallicities in the spectral fitting. The abundance gradient in M101 has been studied extensively using gas phase abundances in HII regions (Garnett et al. 1999; Garnett & Kennicut 1994; Garnett 1989; Torres-Piembert et al. 1989; Evans 1986), yielding either abundance trends (He, N, O, S) or mean abundances (C, Ne, Ar). For the region covered by the *Chandra* observation, the abundances are close to solar for these elements. The nucleosynthetic studies of Timmes et al. (1995) and Alibés et al. (2001), which contain compendia of Galactic abundance data in the form of X/Fe as a function of Fe/H, can be used to link the observed species to those of interest for X-ray spectroscopy, e.g, Ca, Si, Fe, and Ni.

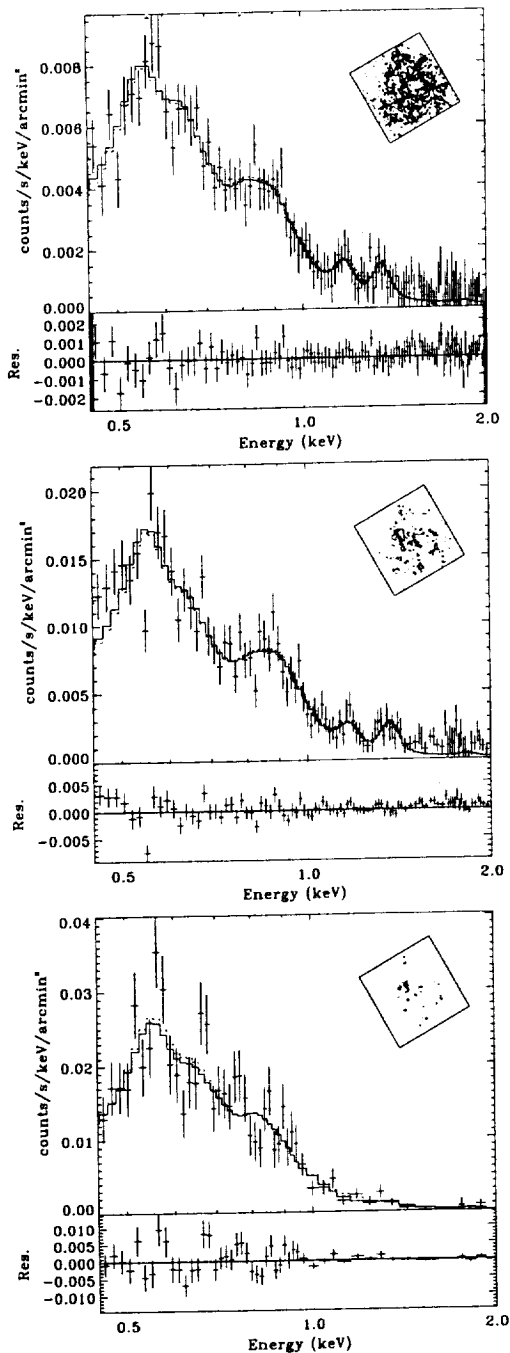We have extracted spectra for three values of surface brightness, A: 1.6-4.8, B: 4.8-8.0, and C:

Fig. 7.— *Top:* Spectrum A, the spectrum for regions with surface brightness 1.6-4.8 $\times 10^{-6}$ counts cm^{-2} s^{-1} arcmin^{-2}. The solid line is the fit assuming no internal absorption, the dotted line is the fit assuming half of the emission is behind the full absorbing column of the disk. The inset shows the region from which the spectrum was extracted. *Middle:* Spectrum B, the spectrum for regions with surface brightness 4.8-8.0 $\times 10^{-6}$ counts cm^{-2} s^{-1} arcmin^{-2}. *Bottom:* Spectrum C, the spectrum for regions with surface brightness 8.0-11.2 $\times 10^{-6}$ counts cm^{-2} s^{-1} arcmin^{-2}.

8.0-11.2 $\times 10^{-6}$ counts cm^{-2} s^{-1} arcmin^{-2} (where the values are above the nominal background). These spectra are shown in Figure 7.

Spectra A and B are well fit with two thermal components, using MeKaL models (Liedahl et al. 1995; Mewe et al. 1986, 1985). That the spectra are fit by two thermal components is not surprising. In the 0.45-1.0 keV interval, there are three major features to be fit: the OVII 0.56 keV line, the OVIII 0.65 keV line, and the 0.7-1.0 keV complex of Fe lines. The Fe complex dominates the fit of the harder component, while the OVII/OVIII ratio dominates the fit of the softer. Our simplest model does not include the effect of absorption internal to M101. A trial fit where the absorption for each component was allowed to vary independently found no absorption for the soft component. The absorption for the hard component was, understandably, poorly determined, with the uncertainty being nearly as large as the fitted value, $\sim 3 \times 10^{21}$i cm^{-2}.

After fitting the two thermal components, there remained two further features at 1.2 and 1.38 keV, as well as a small amount of flux below 1.65 keV. Above 1.65 keV, the Si Kα line from the particle background, though well removed, substantially increases the uncertainty. Above 2.0 keV there is no significant flux. Examination of Figure 6 shows that, while the 1.2 keV feature may be augmented by poor background subtraction, neither feature is produced by the background subtraction process. Non-equilibrium models were no more adequate at fitting these lines than MeKaL models. Due to the small number of counts in this energy interval, the spatial distribution of this contribution can be determined only from very heavily smoothed images (FWHM$\sim$ 32''). The distribution of the 1.1-1.65 keV emission is poorly correlated with the 0.45-1.0 keV emission, which contains the bulk of the galactic emission. Although 1.1-1.65 keV emission is typically found where the 0.45-1.0 keV emission is strong, it is also found where there is little 0.45-1.0 keV emission. The 2.5-5.0 keV emission should contain no galactic emission, and should be composed primarily of the particle background; the 1.1-1.65 keV emission is not correlated with the 2.5-5.0 keV either. To account for these features in fitting, they were modeled as unresolved lines; Gaussians with only instrumental broadening.

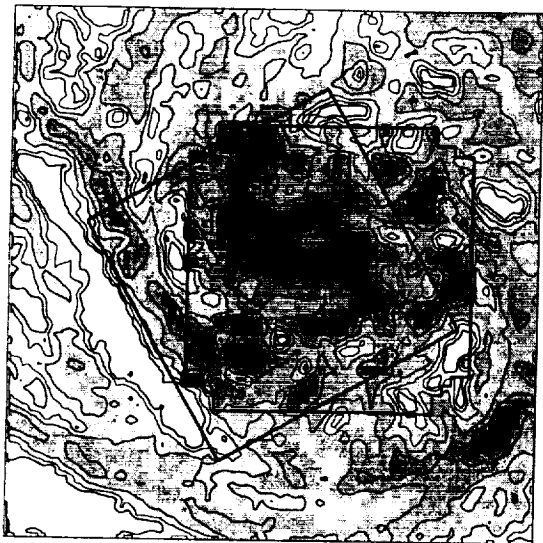In order to estimate the effects of internal ab-

9

Fig. 8.— The total absorbing column. The contours are logarithmic from 10^{20} to 3.2×10^{21} cm^{-2} in steps of $10^{0.25}$. The heavy lines show the location of the *Chandra* image and the area covered by the CO map. With the exception of the giant HII regions, the bulk of the region containing X-ray emission is covered by the CO map.

sorption on the spectral parameters, we fit the spectra both assuming no internal absorption and assuming that half of the emission is behind the disk absorption. The fit parameters are listed in Table 2. The map of total absorbing column was constructed from the 30″ resolution HI map of Kamphuis (1993) and a 55″ resolution CO map kindly provided by T. Helfer. A map of the total absorbing column density is shown in Figure 8. The CO map does not cover the entire area observed by *Chandra*, but does cover the area containing the bulk of the emission. A model assuming that half of the emission is behind the absorption due to the M101 disk typically reduces the temperature of the soft component by $\sim .005$ keV, increases the total soft emission measure by $\sim 87\%$, reduces the temperature of the hard component by $\sim .009$ keV, and increases the total hard emission measure by $\sim 60\%$.

The temperature of the soft component is similar to that found by Wang et al. (1999) (0.186 keV) from a joint *ROSAT* PSPC - *ASCA* GIS fit. Likely as a result of a factor of ~ 3 better spectral resolution, we do not see evidence for their

hotter component ($kT \geq 5.1$ keV), and fixing our hard component to $kT = 5.1$ keV produces a significantly poorer fit ($\Delta\chi^2 = 28$).

3.2.1. Joint Fits with ROSAT

Given that *ROSAT* has a much stronger soft response, and softer components could contribute to the OVII emission. These softer component, not visible to *Chandra* could change the temperatures of the components fitted to the *Chandra* spectrum. We attempted to determine whether the *Chandra* fit was consistent with the *ROSAT* data.

From the *ROSAT* data we extracted the region covered by the *Chandra* chip S3, but not including the giant HII regions or a small region around the nucleus. The background was derived from an annulus between 25′ and 50′, beyond the observed M101 emission. The raw source spectrum contained 3769 counts, of which 2538 were due to the particle background and Galactic foreground. The comparable *Chandra* spectrum was created in two parts. First, we extracted and fit the spectrum for all of the regions containing point sources, excluding source P98 (since P98 is brighter than all of the other point sources combined, and was clearly not visible during the *ROSAT* exposure). The point source contribution was reasonably well modeled by a powerlaw with $\Gamma = 1.6$ and $N_H = 4 \times 10^{20}$ cm^{-2}. Second, we extracted and fit the diffuse emission from the remainder of the chip, excluding the point sources, the giant HII regions, and a small region around the nucleus. For both the *Chandra* and *ROSAT* spectra, the contribution of the unresolved extragalactic background was calculated and removed.

The combined model is shown in Figure 9. The normalization of the *Chandra* model above the carbon edge (primarily the contribution from the diffuse emission) appears to be slightly too high, but within the uncertainties of the individual data points. Below the carbon edge (*ROSAT* bands R1 and R2, the "$\frac{1}{4}$ keV" emission), the emission is split nearly evenly between point sources and the diffuse component. There remains significant emission below the carbon edge that is not accounted for by the *Chandra* model. In joint fits of the *ROSAT* and *Chandra* data, the temperature of the soft *Chandra* component remained well constrained, but neither the very soft component seen only by *ROSAT* nor the harder *Chandra* com-

TABLE 2

SPECTRAL FIT PARAMETERS

Spectrum	Counts[a]	$\overline{R}$ kpc	$N_{nucleon}$[b] 10^{20} cm^{-2}	T_S kT	EM$_S$ $\times 10^{-2}$ cm^{-6} pc	T_H kT	EM$_H$ $\times 10^{-3}$ cm^{-6} pc	χ_ν	ν
A	12907/5582	5.64	0.0	.210 ± 0.015	1.75 ± .17	.741 ± .048	5.94 ± 1.06	0.71	97
			0.0,3.2	.203 ± .013	1.31 ± .11	.730 ± .080	3.46 ± .54	0.71	97
B	4459/1231	4.80	0.0	.195 ± 0.010	3.72 ± .28	.754 ± .066	13.3 ± .2	1.56	85
			0.0,14.2	.190 ± .009	2.87 ± .20	.752 ± .073	7.77 ± .97	1.55	85
C	1442/315	4.76	0.0	.197 ± .021	5.66 ± .67	.607 ± .117	17.6 ± .6	1.36	43
			0.0,15.4	.194 ± .018	4.58 ± .63	.599 ± .101	9.95 ± .47	1.37	43
A+B	17366/6813	5.49	0.0	.204 ± .010	2.11 ± .14	.746 ± .060	7.56 ± .91	0.85	97
			0.0,13.1	.198 ± .012	1.59 ± .11	.732 ± .064	4.23 ± .54	0.86	97
ROSAT[c]	23872/16640	7.03	0.0	.215 ± .028	.745 ± .135	.695 ± .210	1.35 ± 1.14	.55	99
			0.0,10.6	.210 ± .025	.540 ± .082	.691 ± .237	.704 ± .576	.55	99
Ext.Nuc.	794/276	1.12	0.0	.198 ± .026	3.48 ± .54	.706 ± .126	8.53 ± 3.56	1.07	32
			0.0,23.3	.196 ± .019	3.06 ± .48	.711 ± .153	4.74 ± 2.84	1.10	32

For any given spectrum, the first line contains the fit assuming all emission to be on the surface of the disk, the second line contains the fit assuming that half of the emission is behind the entire absorbing column of the disk. The two values of the column density denote the absorption applied to each half of the emission. All uncertainties are 90% confidence intervals.

[a]The first number is the number of raw counts in 0.45-2.0 keV, the second number is the calculated number of particle background counts in the same energy interval.

[b]The column density of hydrogen nucleons was fixed. All absorption is exclusive of the 9×10^{19} cm^{-2} due to the Milky Way.

[c]Region used for comparison with ROSAT.

ponent were well constrained. Assuming that the fit to the *Chandra* spectra was a good model of reality, we fitted the very soft component in the *ROSAT* data and found the 90% confidence interval to be $kT < 0.053$ ($logT = 5.79$), and the 68% confidence interval for the normalization to include zero.

Given the small number of counts, the difficulty of background subtraction below the carbon edge, and the uncertainty of the *ROSAT* calibration at the extreme low energy boundary, one can confidently state only that there appears to be some excess emission below 0.35 keV. One can not completely eliminate the possibility that the softer component seen by *Chandra* does, in fact, contain contributions by even softer components. The similarity of the upper limit of the very soft component to the temperature derived by Snowden & Pietsch (1995) from the *ROSAT* R2/R1 band ratio is surprising, and likely coincidental, given that such a large portion of the $\frac{1}{4}$ keV emission is due to point sources (§3.1.2).

4. Small-Scale Diffuse Emission

4.1. Nucleus/Bulge

M101 has a large-scale bar in CO (J=1→0) emission (Kenney et al. 1991), which is marked in Figure 1. It has a position angle of $102° \pm 4°$, has a length of 1.5 ± 0.5, and appears to "anchor" the main optically defined inner arms. At higher resolution (2″), M101 is a classic "twin-peak" source, with strong CO emission from two compact regions flanking the nucleus where the flow of molecular gas down the bar crosses the ILR Kenney et al. (1992). The two peaks are separated by ~ 3.5 and have a position angle of roughly -10°. In the CO images there are filaments stretching from the twin peaks outwards, roughly along the bar[3]. There is no CO concentration associated with the nucleus.

A similar morphology is seen in Hα (Moody et al. 1995). The (presumed) nucleus is bright in

[3]Note that the position angle of the bar described in (Kenney et al. 1991) is rotated by $\sim 25°$ from the bar described in Kenney et al. (1992).
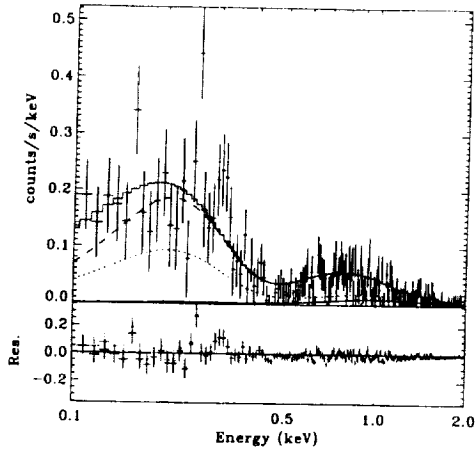
Fig. 9.— The *ROSAT* spectrum of the region covered by the *Chandra* S3 chip. The smooth solid line is the contribution by the unresolved extragalactic background. The dotted line is the contribution by the point sources detected in the *Chandra* image. The dashed line is the sum of the *Chandra* model of the diffuse emission and the previous two components. The stepped solid line is the previous spectrum with the addition of the fitted "*ROSAT*" component. The residuals plotted are from the fit containing the "*ROSAT*" component. The grey residuals are from the *Chandra* model alone.

Hα, and is flanked by two peaks of emission $2''4 \pm 0''15$ from the nucleus (further out than the CO peaks) at a position angle of $+10°$. A strong Hα filament coincides with the southern CO filament, and some Hα features coincide with an extension of the northern CO filament. A WFPC I image ($\lambda5479$) on PC chip 6 shows a bright point-like source at the position of the southern Hα peak, but no northern counterpart (Moody et al. 1995).

Figure 10 shows the nuclear region of our *Chandra* observation smoothed by $1''968$ (4 ACIS pixels) HWHM gaussian. Pence et al. (2001) used optical SNR to tie the X-ray coordinate system to the optical coordinate system of Matonick & Fesen (1997), and found that the *Chandra* coordinates need be corrected by an offset of $0''47 \pm 0''20$, less than the size of an ACIS pixel. Boxes mark X-ray point sources; the position uncertainties are significantly smaller than the marked boxes. The separation of the two nuclear sources is $3''16$.
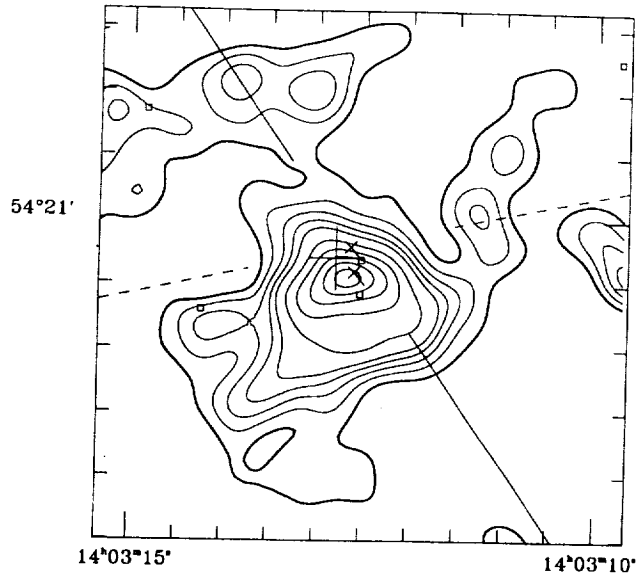
The large cross is the position and uncertainty

Fig. 10.— The nuclear region. The X-ray contours are $[1, 1.5, 2.0, 2.5, 3, 4, 5, 6, 7, 8] \times 10^{-5}$ counts cm^{-2} s^{-1} $arcmin^{-2}$. The image has been smoothed by a $3''97$ FWHM Gaussian. The solid straight line is the line of nodes, the northwest corner is towards the observer. The dashed straight line is the orientation of the molecular bar. The cross shows the location and uncertainty of the Israel et al. (1975) position of the radio continuum nucleus. The upper × is the position of the optical nucleus from a WFPC I image; the lower × is the position of the southern optical/Hα source. The small boxes are the X-ray point sources. The non-systematic uncertainties of the positions of the optical and X-ray sources is much smaller than the plot symbols.

of the continuum nuclear source (Israel et al. 1975), and the dynamical center determined from the CO (Kenney et al. 1991). The upper "×" is the optical nucleus and the lower "×" is the southern optical/Hα source. The non-systematic uncertainty for the optical sources is also very small on this figure. Both optical sources, the northern X-ray source, and the peak of the diffuse X-ray emission are within the positional uncertainty for the continuum nucleus. The long tails on the optical symbols show the shift necessary to make the optical nucleus coincide with the northern X-ray source; if the northern X-ray source is the optical nucleus, the southern X-ray source does not coincide with the southern Hα source.

12

Since both the northern and southern nuclear X-ray sources have spectra consistent with that of rather ordinary X-ray binaries, their locations may be coincidental. This region is dynamically interesting, and might be expected to shed light on the complex occurences at the center of our own Galaxy. If we take the *HST* and *Chandra* astrometry at face value, the bulk of the diffuse X-ray emission is centered near the southern optical/Hα source, which, given its proximity to the CO peak, might be expected to be a region of intense star formation. Given the extended nature of the emission and the position of the line of nodes, the lack of a northern counterpart is curious. Conversely, a $\sim 1{.}''5$ shift, somewhat larger than the expected *HST*/*Chandra* r.m.s. offset ($\lesssim 1{.}''2$), could make the optical nucleus coincident with the northern X-ray source.

Our understanding of the nucleus is hampered by the lack of a good independent measure of the offset in the optical and X-ray coordinate systems. This measure will come with the execution of a survey of M101 with the *HST ACS* in November 2002, which will attempt to identify the X-ray sources over the entire ACIS-S3 field with optical counterparts.

4.1.1. Spectroscopy

We extracted spectra from the nuclear region at two different surface brightness levels. From the compact nucleus itself we extracted the region with surface brightness $> 1.7 \times 10^{-5}$ counts cm^{-2} s^{-1} arcmin^{-2} shown by the higher thick contour in Figure 11. The mean column density for this region is 2.8×10^{21} cm^{-2}, the bulk of which (2.6×10^{21} cm^{-2}) is due to molecular gas. Although the nucleus itself is quite bright, the total number of counts is still small (239 counts in 0.11 arcmin^2). The spectrum is reasonably fit by an absorbed Bremsstrahlung, $N_H = 1.8 \times 10^{21}$ cm^{-2}, $kT = 0.262$ keV, $\chi_\nu = 0.58$ for $\nu = 10$ (Figure 11b). Other spectral forms (power law, thermal plasmas, etc.) produced worse fits.

We extracted the spectrum of the extended emission around the nucleus, the region with surface brightness 0.725×10^{-5} counts cm^{-2} s^{-1} arcmin$^{-2} < S < 1.7 \times 10^{-5}$ counts cm^{-2} s^{-1} arcmin^{-2}; between the two thick contours in Figure 11. The mean column density for this region is 2.3×10^{21} cm^{-2}, the bulk of which (2.2×10^{21}
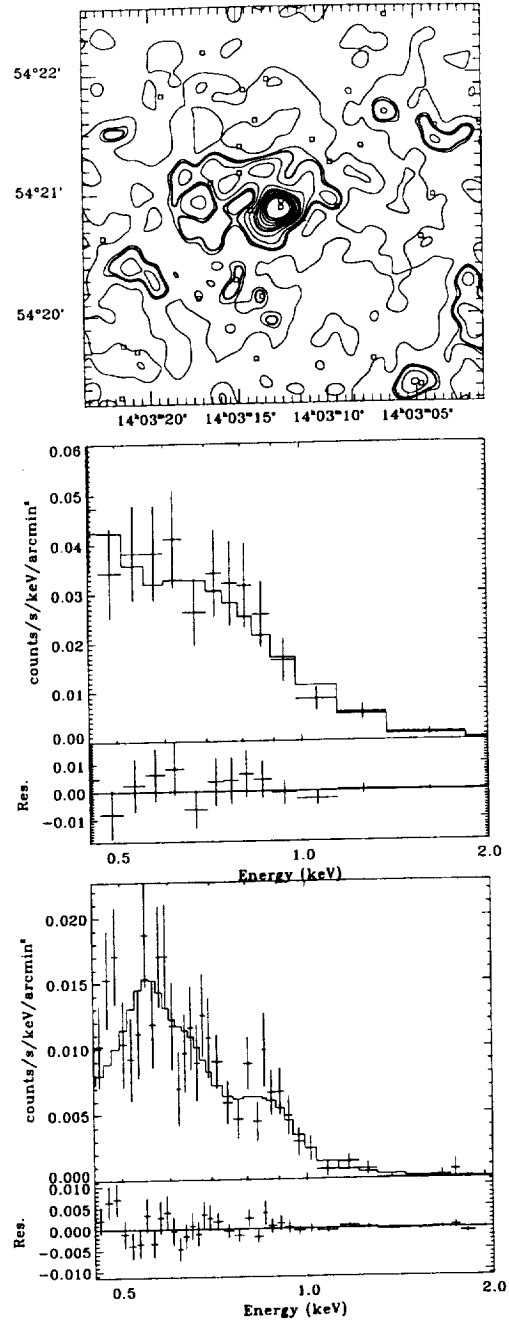

Fig. 11.— *Top:* The extended nuclear region. The smoothing is the same as in Figure 1 (twice as much as in figure 10). The contours are from 0.32×10^{-5} counts cm^{-2} s^{-1} arcmin^{-2} to 3.2×10^{-5} counts cm^{-2} s^{-1} arcmin^{-2} in steps of 0.32×10^{-5} counts cm^{-2} s^{-1} arcmin^{-2}. The dark contours at 0.725 and 1.7×10^{-5} counts cm^{-2} s^{-1} arcmin^{-2} delimit the regions from which spectra were extracted. *Middle:* The spectrum for the region with surface brightness greater than 1.7×10^{-5} counts cm^{-2} s^{-1} arcmin^{-2}. *Bottom:* The spectrum for the region with $7.25 \times 10^{-6} <$ surface brightness$< 1.7 \times 10^{-5}$ counts cm^{-2} s^{-1} arcmin^{-2}.

13

cm^{-2}) is due to molecular gas. This spectrum (Figure 11c) can be fit with a two thermal components (see ext.nuc. line in Table 2). Although we allowed the absorption to vary independently for the components, the fitted absorption was consistent with no absorption for either component. Including a Bremsstrahlung component as a contaminant from the nucleus changes the thermal temperature and reduces the normalizations, but only slightly.

Thus, as the nuclear emission appears to be absorbed by about half of the total column density, it seems reasonable that the nucleus itself is embedded in the molecular ISM of the bar. The extended nuclear emission appears to be mostly unabsorbed, and is likely extraplanar. Assuming that half of the extended nuclear emission is behind the column density measured in HI and CO does not significantly change the goodness of the fits or the fitted temperatures.

4.2. Giant HII Regions

Three giant HII regions fall on the S3 chip (see Figure 1). Of these, NGC 5453 was not detected by either *ROSAT* PSPC (Williams & Chu 1995) or HRI (Wang et al. 1999) surveys. In this *Chandra* image there is a very faint enhancement partially encircling the listed position. NGC 5462 falls on the part of the chip with the worst PSF, and the PSF for NGC 5461 is only slightly better.

Both NGC 5461 and NGC 5462 were studied by Williams & Chu (1995) who found them resolved by the PSPC, but due to contamination by the soft extended disk emission they could not rule out the presence of a single large X-ray source producing the X-ray emission from each region. Despite the relative softness of HII regions, both of these objects show extended emission in the deep HRI survey by Wang et al. (1999) In the *Chandra* image, both NGC 5461 and NGC 5462 show diffuse extended emission as well as bright point sources.

NGC 5462: The spectrum was extracted from a region with a surface brightness greater than 3.3×10^{-6} counts cm^{-2} s^{-1} arcmin^{-2}. The diffuse emission is reasonably fit ($\chi^2_\nu = 0.97$) by an absorbed MeKaL model. A somewhat better fit ($\chi^2_\nu = 1.2$) can be found by assuming the sum of an unabsorbed thermal component and an absorbed thermal component, the same type of model that
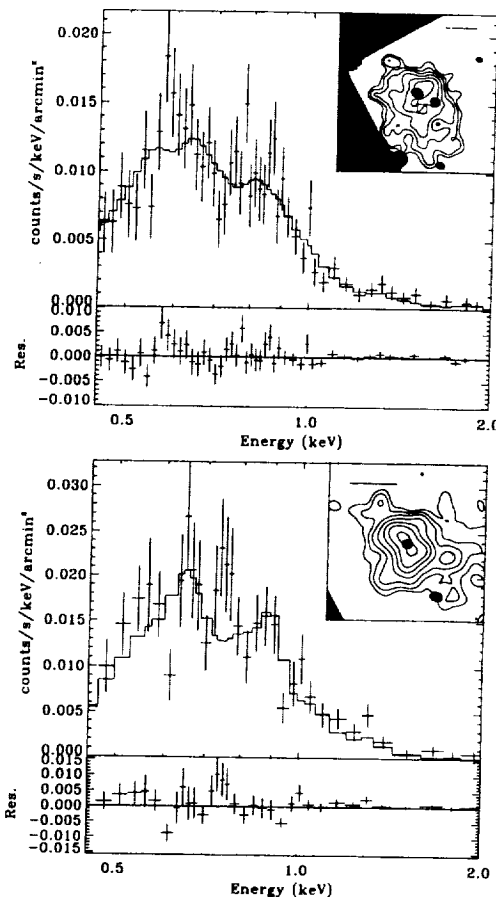
Fig. 12.— *Top:* Spectrum of NGC 5462. The model spectrum is the sum of an unabsorbed MeKaL thermal component and an absorbed MeKaL component. The inset image contours are 2.4, 4.0, 6.3, 10., 16., 24. $\times 10^{-6}$ counts cm^{-2} s^{-1} arcmin^{-2}. The black regions are either off-chip or removed for point sources. The scale bar is 30″ long. The box is the location of SN 1951H. *Bottom:* Spectrum of NGC 5461. The model spectrum is an absorbed MeKaL thermal model.

14

fits the disk emission. (See Table 3.) In this case, the temperature of the unabsorbed component is well-constrained and similar to the soft disk component; the absorbed component is not well-constrained, but is clearly hotter. A fit containing an unabsorbed MeKaL component and an absorbed power law is significantly worse, implying that the non-thermal component is small. Extracting a spectrum using a higher surface brightness cut did not significantly change the fits. The supernova remnant SN 1951H is offset from the X-ray center, but is within the extended emission. Given that a giant HII region is likely to be formed of many different X-ray emitting components, expanding hot stellar wind bubbles, SNR, etc., and given the small number of counts in this spectrum, the poorness of the fit is not surprising.

NGC 5461: The diffuse emission is reasonably fit ($\chi_\nu^2 = 1.58$) by an absorbed MeKaL model. As with NGC 5462, a somewhat better fit ($\chi_\nu^2 = 1.2$) can be found by assuming the sum of an unabsorbed thermal component and an absorbed thermal component, but the fit parameters are poorly constrained.

5. Discussion

Observations such as those discussed in this paper stand at the curious intersection of disciplines: between the theory of galaxy formation and the classical study of the ISM, between processes dominated by the depth and shape of the dark matter potential and processes dominated by the dynamical mixing of the ISM by star formation. We attempt here to place these observations into the context of both disciplines, and begin by comparing M101 to the well-known but not so well-understood ISM laboratory that is the Milky Way.

M101 is larger than the Milky Way, having a D_{25} about twice that of the Galaxy, but has only about half the mass of the Milky Way, though with a larger mass fraction in neutral gas (see Table 1). The far-infrared luminosity, a very crude measure of the star formation rate, is about that estimated for the Galaxy, implying that the star formation rate per disk area, or per gas mass, is substantially lower than the Galactic rate. Comparing M101 for which $L_{FIR}/D_{25}^2 = 1.37 \times 10^{40}$ ergs s^{-1} kpc^{-2} to the list of that quantity for edge-on spirals from Rand (1998), and the correlation with extraplanar

diffuse ionized gas, one can see that M101 is not expected to have a very extended "DIG" layer. This is not to say that star formation in M101 is in any way "quiescent"; the several giant HII regions are more reminiscent of those in the Magellanic Clouds than the star forming regions seen in the Milky Way.

The M101 ISM may be quite similar to that of the Milky Way. Kregel et al. (2002), using the work of Bottema (1993) has noted that the stellar velocity dispersion perpendicular to the disk is equivalent to the scaled circular v_{max}. For spiral galaxies, the scale height of the old stellar population is nearly constant with radius (e.g., van der Kruit & Searle 1982). Thus, from the optical B-band profile (Okamura et al. 1976), the HI rotation curve and vertical velocity dispersion profile (Kamphuis 1993), and using the formulary of van der Kruit (1988), one can calculate the mid-plane density of the neutral gas, and finds $\rho_0 \sim 0.35$ cm^{-3} for the radii of interest (4-8 kpc). This value is similar to the mid-plane density of neutral gas in the solar neighborhood (0.22-0.38 cm^{-3}, Lockman & Gehman 1991). (The calculation uses the thin disk approximation which is valid for regions with a flat rotation curve; the rotation curve for M101 is gently rising at the radii, so the results must be viewed with some skepticism.) If one assumes that the M101 disk has a similar CNM/WNM/WIM structure as the Milky Way, then given the similar neutral gas density, one would expect the hot structures, if they are at all pressure confined, to have properties similar to those in the Milky Way.

The prime difficulty with observing hot gas within the Milky Way is the high absorbing columns built up over lines of sight within the disk that limit our view of the Galaxy to the nearest .5-1.5 kpc at $0.5 < E < 1.0$, and even shorter distances at lower energies. The filling factor of X-ray emitting gas within the disk is thus a hotly debated topic. We know of several small isolated examples of bubbles of $\sim 10^6$ K gas (Snowden 2001), and one example of a superbubble filled with $\sim 2 \times 10^6$ K gas (Egger 1993). At higher energies, where we sample more of the Galactic disk, several hot Galactic ridge components have been identified (e.g., Kaneda et al. 1997, with $kT = 0.8$ and $kT = 7$) but their luminosities and filling factors are poorly known.

15

TABLE 3

SPECTRAL FIT PARAMETERS

Region	Counts[a] (0.45-2.0) keV	Area arcmin^2	N_H 10^{20} cm^{-2}	T_1 kT	EM_1 cm^{-6} pc	N_H 10^{20} cm^{-2}	T_2 kT	EM_2 cm^{-6} pc	χ_ν	ν
NGC 5461	706/149	0.607	65^{+7}_{-16}	$.155^{+.038}_{-.014}$	$7.2^{+8.0}_{-5.7}$				1.58	29
			$.9*$	$.261^{+.034}_{-.219}$	$.048^{+.005}_{-.024}$	125^{+129}_{-49}	$.178^{+.406}_{-.115}$	$10.0^{+4805}_{-9.9}$	1.23	27
NGC 5462	1199/331	1.518	54^{+10}_{-8}	$.175^{+.013}_{-.028}$	$1.8^{+4.2}_{-0.9}$				.968	47
			$.9*$	$.241^{+.026}_{-.021}$	$.033^{+.006}_{-.006}$	407^{+207}_{-294}	$.654^{+.351}_{-.136}$	$.043^{+.036}_{-.023}$	.938	45

Quantities with asterisks are fixed. All uncertainties are 90% confidence intervals.

[a]The first number is the raw counts in 0.45-2.0 keV, the second is the calculated number of particle background counts.

About our halo we know a little more. Using the *ROSAT* All-Sky Survey, Kuntz & Snowden (2000) divided the Galactic halo emission into two components, a hard component ($kT = 0.250^{+.079}_{-.045}$) whose intensity remains constant across the high latitude sky, and a patchy soft component ($kT = 0.098^{+.055}_{-.037}$). (Whether these temperatures will survive the higher spectral resolution of the *Chandra* and *XMM-Newton* era is a topic of ongoing research.) The extraplanar X-ray emission from the Galactic bulge has been modeled as a cylinder of radius 5.6 kpc having an exponential scale-height of 1.9 kpc and a temperature ▓▓▓ = .343 (Snowden et al. 1997).

In M101, of course, we are observing both disk and halo gas. Assuming that half of the emission is behind the absorption of the galactic disk, the total luminosity of diffuse emission is 1.53×10^{39} ergs s^{-1} and 0.73×10^{39} ergs s^{-1} in 0.45-2.0 keV for the $kT = 0.2$ keV and $kT = 0.7$ keV components. The total luminosity of these two components is $\sim .3\%$ of the supernova luminosity, assuming 2 supernovae per century (Matonick & Fesen 1997).

5.1. Disk

The bulk of the disk of M101 is covered by low surface brightness X-ray emission which traces the spiral arms. The low surface brightness emission in M101 appears to consist of two different components, and the constancy of the hardness ratio shows that the relative amounts of these two components is relatively constant for the bulk of the emission. This uniformity suggests that the sources of the two components are linked to one another, and to star formation. A similar two-component medium is seen in the spectrum of the actively star-forming galaxy NGC 2403 (Scd), where the best fit two MeKaL-component model has temperatures of $kT = 0.18 \pm 0.03$ and $kT = 0.73 \pm 0.07$ (Fraternali et al. 2002), while the early-type spiral NGC 1291 (Sa) appears to have a single thermal component with a temperature $kT = 0.33$ keV (Irwin et al. 2002). As the diffuse emission is analyzed for similar galaxies in the *Chandra* and *XMM-Newton* archive, such two component media may become a mark of late-type disks.

The softer component in M101 has a temperature of ~ 0.2 keV. This is similar to the temperature found for superbubbles such as those in the Magellanic Clouds or that outlined by the Galactic Loop I. The brightest portion of the Loop I superbubble, a shock front seen obliquely, has $kT = 0.17 - 0.30$ and an emission measure of 0.02-0.04 cm^{-6} pc (Egger & Aschenbach 1995)). The emission measure of the softer component of the M101 disk is similar, 0.018-0.038 cm^{-6} pc, suggesting a covering fraction near unity for superbubbles, or, more reasonably, that a substantial amount of the gas is actually in the halo. An object similar to the Loop I superbubble (radius=150 pc) would subtend an angle of $4''3$ at the distance of M101, and have a surface brightness of $\sim 3 \times 10^{-3}$ counts cm^{-2} s^{-1} arcmin^{-2}. Due to its small size, after the smoothing applied to produce the data shown in Figure 1, it would have a surface brightness of only $\sim 3 \times 10^{-6}$ counts cm^{-2} s^{-1} arcmin^{-2}. In the presence of other diffuse emission, the Loop I superbubble would be

16

undistinguishable in the disk of M101.

It is interesting to note that unlike NGC 2403, where the sound speed of the softer component was comfortably below the escape speed, in M101 the sound speed of the softer component $((\gamma kT/\mu m_p)^{\frac{1}{2}} \sim 230$ km s^{-1}) is just barely compatible with the escape velocity ($\sqrt{2}v_c \sim 240$ km s^{-1}). However, this simple comparison should not be taken as indicating that the gas is escaping the galaxy. Breitschwerdt & Schmutzler (1999) modeled galactic chimney flows in a dynamically self-consistent manner and found that the adiabatic expansion of the gas out of the disk cools the gas significantly, but leaves a much higher, non-equilibrium ionization structure frozen into the gas. Their model starts with an initial CIE gas at 2.5×10^6 K, but the gas cools rapidly with increasing height above the disk to $\sim 10^4$ K, but the gas has a spectrum more similar to that of a 10^6 K gas. Given that the bulk of the temperature information for the soft component is derived from the ratio of the oxygen lines, our temperature may not indicate the true gas temperature, but only the ionization temperature of the oxygen.

Kahn (1990, 1997) has placed a more restrictive constraint on this gas. Calculations for the Galaxy shows that the galactic chimney/fountain gas cools long before reaching the scale height indicated by its initial temperature, a result confirmed by the modeling of de Avillez (2000). Thus, the fountain gas is supported dynamically, does not fill the potential well, and does not produce a quasi-hydrostatic halo.

If one *does* assume that the soft component has an exponential scale-height $kT/\mu m_p g$, where $g = 4\pi G\Sigma$, and Σ is the surface mass density (derived from the optical B-band profile under the assumption that the mass-to-light ratio is similar to that of the solar neighborhood, $\Upsilon_B = 2.3$ M$_\odot$L$_\odot^{-1}$) then the peak electron density is 2-3×10^{-3} cm^{-3} at radii of ~ 5 kpc. This value is 2 to 3 times smaller than the n_e derived for the Local Hot Bubble ($n_e = .006$ cm^{-3}, $kT = .108$ keV), and ~ 5 times smaller than the densities derived either from the Eridion Bubble ($n_e \sim .015$, cm^{-3}, $kT = .17$ keV Guo et al. 1995) or the walls of the Loop I superbubble ($n_e \sim .01$-.015 cm^{-3}, Egger 1993), but is similar to the tenuous medium filling the center of the Loop I superbubble ($n_e = 3 \times 10^{-3}$ cm^{-3} Egger 1993). Given the softness of the Local Hot
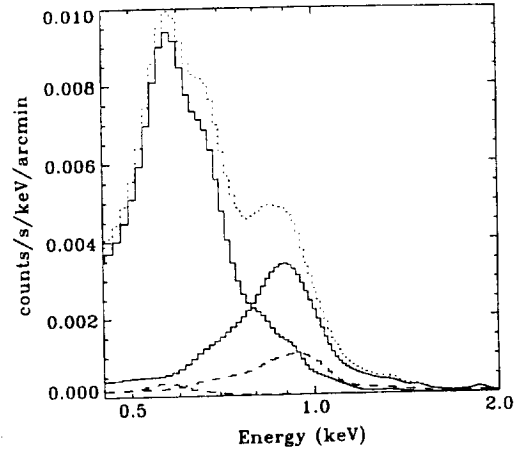

Fig. 13.— *Dotted:* The model spectrum fit to spectrum A+B. *Solid:* The soft and hard thermal (MeKaL) components. *Dashed:* The contribution by dwarf stars to the soft and hard components.

Bubble and its overburden (typically a few ×10^{20} cm^{-2}), similar objects in M101 will not contribute substantially to the *Chandra* spectrum. Assuming that the soft component is formed by a population of objects such as the Loop I Bubble or the Eridion Bubble, and assuming that such objects have a signficant z extent, the filling fraction of hot gas would be ~ 0.2.

If, instead, one assumes the Breitschwerdt & Schmutzler (1999) model, then the amount of truly hot gas will be a fraction of the amount indicated by the X-ray flux. Using the approximation that the flux $\propto 1/z$ given in Breitschwerdt & Schmutzler (1999) one finds about .3 of the total flux is due to truly hot gas. Since the fraction of the total flux falling within the *Chandra* bandpass may vary with z-height, a better estimate must wait for detailed modeling.

The harder component has a temperature of ~ 0.7 keV. This temperature is similar to that expected from the aggregate emission due to late-type dwarf stars ($kT \sim 0.8$ keV). We have used a model similar to that used by Kuntz & Snowden (2001) to calculate the emission by dwarfs (spectral types F through M) per square parsec in the solar neighborhood, and scaled the result by the disk surface mass density. It should be noted that while the Kuntz & Snowden (2001) model was

17

normalized to the number of K and M dwarfs in the solar neighborhood, and matched the number of Galactic stellar X-ray sources at high Galactic latitude, it did not match the mid-plane stellar mass density. Further, the Kuntz & Snowden (2001) model, since it matched the number counts at high Galactic latitude, was not sensitive to the substantial uncertainties in the X-ray luminosities of young stars, whereas a sum through the entire disk is quite sensitive; even though there are one-tenth the M dwarfs in the 0.0-0.1 Gyr age range as in the 1-10 Gyr range, their X-ray luminosities are ten times greater, so their contribution to the X-ray emission is comparable. Thus, considering the uncertainty with which one can apply the Galactic IMF and SFR to M101, the calculation of the contribution of dwarf stars to the X-ray emission in M101 is a rather uncertain estimate. We find that dwarf stars account for $\sim 35\%$ of the 0.45-2.0 keV band flux of the harder component, only $\sim 2\%$ of the softer component, and $\sim 11\%$ of the total flux.

The temperature of the harder *Chandra* component is also similar to the "soft" Galactic component ($kT = 0.8$ keV) found by Kaneda et al. (1997) in their *ASCA* study of the Scutum arm. (Note that their "soft" component is much harder than the "hard" component of Kuntz & Snowden (2000).) In their case, the spectrum was modeled with a non-equilibrium model requiring $n_e t = 10^{9.1}$ cm^{-3} s. Replacing our hard MeKaL component with an NEI component does little to change the fit and requires $n_e t = 10^{12.9}$ cm^{-3} s, that is, nearly an equilibrium plasma. From the fitted value of the absorbing column, Kaneda et al. (1997) estimate that the effective distance to the Galactic region producing their soft emission to be ~ 2 kpc, and find a scale height of 100 pc. If their emission is produced along a 2 kpc line of sight then the expected emission from M101 would be 1.9×10^{-7} ergs cm^2 s^{-1} sr^{-1}; the observed value for the hard component of the A+B spectrum is 4.7×10^{-8} ergs cm^2 s^{-1} sr^{-1}, only a factor of four smaller. If the Kaneda et al. (1997) emission is over a longer path, then the two values would be more similar. The harder component found by Kaneda et al. (1997) ($kT \sim 7$ keV) is too dim to be observed by *Chandra* at the distance of M101.

Kaneda et al. (1997) attributed their 0.8 keV component to late stage supernovae expanding into regions of low ambient density, conjecturing

that supernovae are abundant, one per GIS field of view, and reheating regions previously swept by older supernovae. Although the M101 equivalent is likely to be produced by the same means as in the Milky Way, the M101 spectra do not posess the evidence for non-equilibrium plasmas that would point to young SNR. Absence of evidence is not, however, evidence of absence, and the presence of such a component may be obscured by other emission components. A further caution concerning the supernova attribution can be derived from the hydrodynamic supernova models of Shelton (1999). In those models of individual supernova in low density ambient media, typical time-averaged temperatures were $\lesssim 0.35$ keV, substantially cooler than the observed component. Greater ambient densities lead to significantly higher emissivities, but not significantly higher temperatures.

In M101, there are likely multiple sources for the hard component. Active star formation regions such as R136 in 30 Dor, for example, can produce hot thermal components with $kT \sim 0.8$ keV (Wang 1999). A covering fraction of .1-.2% by 30 Dor-like objects could provide the observed emission measure for the hard component, but would over-produce the soft emission by a factor of ~ 5.

Two Component Structure: As has been mentioned previously, it is not surprising that the spectrum is statistically well fit by two components in collisional ionization equilibrium. The emission occupies only a small range of the energy interval accessible to *Chandra*, 0.45 to 1.0 keV, with a resolution of 0.12 keV. Within this energy interval, the emission is dominated by the OVII/OVIII lines at .560 and .650 keV, and the Fe complex at 0.7-1.0 keV. The softer component produces the bulk of the oxygen flux, while the harder component produces the Fe emission. A range of temperatures probably exists, but we are determining the most common gas temperatures.

A similar problem was experienced by the even lower resolution *ROSAT* studies of the Galactic halo. Kuntz & Snowden (2000) suggested that the temperatures of the two Galactic halo components might be indicative of an isochorically cooling gas which passes through two regions of increased stability on its path down the cooling curve, an argument analogous to that made by Gehrels & Williams (1993) to explain the bimodal

temperature distribution of emission from RS Can Ven stars.

Such an argument has a more limited applicability in this case. The cooling curve derived from the Raymond & Smith (1977) model allows regions of relative stability at kT=0.068-0.121 (0.79-1.4×10^6 K) and kT=0.388-0.646 (4.5-7.5×10^6 K), and similar results are obtained from APED (Smith et al. 2001) models (Smith 2002). Significantly altering the metallicities does change the location of the inflection points, but not significantly for the range of metallicities observed in M101. The temperature of the soft component falls several σ above the lower inflection. The temperature of the hard component is marginally incompatible with the upper limit. However, as very hot gas produced in the disk is not likely to cool isochorically, and the isobaric cooling curve does not have regions of enhanced stability, the temperature of the upper component is unlikely to be due to the cooling curve.

5.2. Bulge

The bulge of M101, as seen in the optical data of Okamura et al. (1976), can be characterized as having an exponential profile with a scale length of 100 pc, much smaller than the bulge of the Galaxy, which has a scale length of $\sim$ 1 kpc. In M101 the extended X-ray nucleus has a scale length similar to that of the optical bulge, and the bulge-to-disk ratio in the X-ray is similar to that of the optical. Given the small size of the bulge and the scaling of the X-ray emission with optical light, it is perhaps not surprising that, unlike the Galaxy, the X-ray emission does not show a marked change in temperature between disk and bulge. In the X-ray range, there are no signs of nuclear activity, and the nuclear point sources are consistent with ordinary X-ray binaries.

5.3. Extended Halos

Since the classic paper by Spitzer (1956), the high energy model of galaxies has included a nearly spherical hot corona or halo, either in hydrostatic equilibrium, or in some similar state. The existance of such a halo seems reasonable given that the virial temperature of a galaxy like the Milky Way is $\sim mv_c^2/2k = 2 \times 10^6$ K, where v_c is the circular velocity. Models of the soft
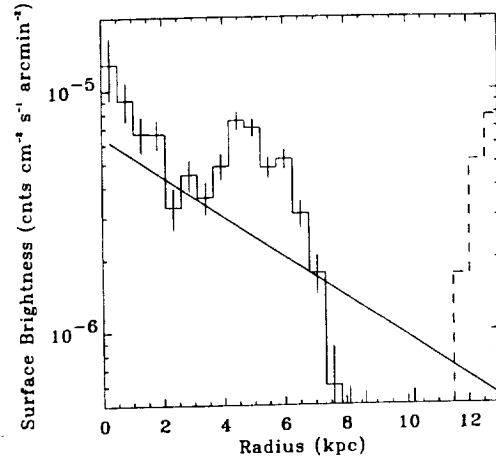

Fig. 14.— The radial profile for position angles 60° to 110°. The solid line excludes the giant HII regions; the dashed line includes the giant HII regions.

X-ray emission from our own Galaxy usually include such a component (Wang 1998; Pietz et al. 1998), though Kuntz & Snowden (2001) suggested that the rather featureless component that dominates the $ROSAT$ $\frac{3}{4}$ keV emission may not be due to a Galactic corona, but rather to cosmological sources.

Observations of other galaxies in the $ROSAT$ era were generally equivocal; the only extended halos detected around non-starburst, edge-on galaxies were arguably due to high star formation rates (NGC 4631 and NGC 891). Benson et al. (2000), noting that simple cooling flow models of galaxies predicted $L_X \propto v_c$, searched for extended X-ray halos around three massive galaxies. Although these galaxies were expected to have $L_X \sim 10^{42}$ ergs cm^{-2} s^{-1}, the observed 95% upper limits were 3.8, 1.2, and 0.4×10^{41}.

Toft et al. (2001), executing SPH models of galaxy formation from $z \sim 20 - 40$ to the present, found their galaxy halos to be at least an order of magnitude fainter than the halos produced by the simple cooling flow models of galaxy formation. M101 is voluminous, but not massive. The $L_X - v_c$ relation found by Toft et al. (2001) suggests that M101 ($v_c \sim 170$ km s^{-1}) should have a halo with $L_X = 1 - 3 \times 10^{38}$ ergs s^{-1} in the 0.2-2.0 keV band, $T \leq 10^6 K$, and the X-ray emission

should be fairly closely confined to the disk.

Figure 14 shows the radial profile of M101 between position angles 60° and 110° (measured from North). At radii greater than ~ 7 kpc, the observed surface brightness drops sharply to the value of the background measured by *ROSAT*; the 2σ upper limit is 9×10^{-16} erg cm^{-2} s^{-1} in 0.45-1.0 keV. Thus any axisymmetric halo must make an insignificant contribution beyond this radius. The Toft et al. (2001) value for halo luminosity is 7-20% of the measured 0.2-2.0 keV luminosity of the diffuse emission within 7′. Since the X-ray luminosity follows the optical luminosity (i.e., Figure 4), and there is no excess X-ray emission within 7′ other than the bulge, the true strength of an X-ray halo not due to disk processes is likely to be much smaller than the 7-20% predicted by Toft et al. (2001). From the viewpoint of ISM studies, this result is the anticipated consequence of galactic fountains.

5.4. Flotsam

Nucleosynthetic studies of the Milky Way suggest that galaxies continue to accrete material, $\sim 1 M_\odot$ year^{-1} for the Galaxy (Alibés et al. 2001; Timmes et al. 1995), and generally cite the (as yet unknown) mass of high velocity clouds as a plausibility argument. The luminosity due to the infalling material should be $\sim 10^{40}$ ergs s^{-1}, five times the observed amount of diffuse X-ray emission in this *Chandra* observation. This point may not be consequential, as estimates for the current infall rate required for nucleosynthesis appears to have at least a factor of three uncertainty (e.g. compare Alibés et al. 2001 with Timmes et al. 1995). Further, given the structure of high velocity clouds, the infall is likely episodic. However, M101 appears to be abundant in high velocity gas, having $\sim 2 \times 10^8$ $M_\odot$ (Kamphuis 1993). Unfortunately, this gas is situated entirely outside of the field of view of this *Chandra* observation; *XMM-Newton* may be able to determine to what low level the high velocity cloud/halo interface shock contributes to the diffuse X-ray emission.

6. Summary

The bulk of the truly diffuse emission from M101 traces the spiral arms and is correlated with Hα and FUV emission, implying that it is due to ongoing star formation: hot winds from massive young stars, supernovae, and superbubbles. The spectrum of the diffuse disk emission is characterized by two thermal components with temperatures $kT = 0.20$ keV and $kT = 0.75$ keV. The ratio of the emission measures is roughly constant across the face of the galaxy with $EM_{soft}/EM_{hard} \sim 3$. Comparison of the temperatures and emission measures of these components to diffuse features in the Galaxy or the Magellanic clouds suggest that a significant fraction of the gas forming the soft component is extraplanar. The hard component in M101 is similar to the soft Galactic ridge component seen in the Milky Way, but has a substantial contribution from dwarf stars.

We do not find evidence for an axisymmetric halo tracing the dark matter potential. At a radius of ~ 7 kpc, the deep interarm region shows no sign of X-ray emission above the level of the background. Given that M101 is a fairly low mass galaxy, the lack of such a halo may not be surprising.

Whether M101 has a true nuclear source remains unknown. The diffuse emission from the highest surface brightness portion of the nucleus has a spectrum consistent with thermal Bremsstrahlung absorbed by about half of the total M101 column density in that direction. The remainder of the nuclear emission has a spectrum consistent with that of the diffuse disk emission.

The giant HII regions NGC 5461 and NGC 5462 are composed of truly diffuse emission whose spectral shape is similar to that of the disk emission, but the total number of counts is too small to allow detailed spectral fitting. The non-thermal component in these spectra appears to be small.

REFERENCES

Alibés, A., Labay, J., & Canal, R. 2001, A&A, 370, 1103

Beck, R., & Golla, G. 1988, A&A, 191, L9

Benson, A. J., Bower, R. G., Frenk, C. S., & White, S. D. M. 2000, MNRAS, 314, 557

Binney, J., & Merrifield, M. 1998, Galactic Astronomy (Princeton University Press)

Bottema, R. 1993, A&A, 275, 16

Breitschwerdt, D., & Schmutzler, T. 1999, A&A, 347, 650

Chen, L.-W., Fabian, A. C., & Gendreau, K. C. 1997, MNRAS, 285, 449

Comte, G., Monnet, G., & Rosado, M. 1979, A&A, 72, 73

Dame, T. M. 1992, in Back to the Galaxy, ed. S. S. Holt & F. Verter, 267

de Avillez, M. A. 2000, MNRAS, 315, 479

Egger, R. 1993, Ph.D. thesis, Technische Universität München

Egger, R., & Aschenbach, B. 1995, A&A, 294, L25

Evans, I. N. 1986, ApJ, 309, 544

Fraternali, F., Vappi, M., Sancisi, R., & Osterloo, T. 2002, ApJ, in press

Fullmer, L., & Lonsdale, C. J. 1989, Catalogued Galaxies and Quasars observed in the IRAS Survey, Version 2 (JPL)

Garnett, D. R. 1989, ApJ, 345, 282

Garnett, D. R., & Kennicut, R. C. 1994, ApJ, 426, 123

Garnett, D. R., Shields, G. A., Peimbert, M., Torres-Piembert, S., Skillman, E. D., Dufour, R. J., Terlevitch, E., & Terlevitch, R. J. 1999, ApJ, 513, 168

Gehrels, N., & Williams, E. D. 1993, ApJ, 418, L25

Guo, Z., Burrows, D. N., Sanders, W. T., Snowden, S. L., & Penprase, B. E. 1995, ApJ, 453, 256

Hartmann, D., & Burton, W. B. 1997, Atlas of Galactic Neutral Hydrogen (Cambridge University)

Hodge, P. W., Gurwell, M., Goldader, J. D., & Kennicutt, R. C. 1990, ApJS, 73, 661

Irwin, J. A., Sarazin, C. L., & Bregman, J. N. 2002, ApJ, 152

Israel, F. P., Goss, W. M., & Allen, R. J. 1975, A&A, 40, 421

Kahn, F. D. 1990, in The Interstellar Disk-Halo Connection in Galaxies, ed. H. Bloemen, 1

Kahn, F. D. 1997, in The Local Bubble and Beyond, ed. D. Breitschwerdt, M. Freyberg, & J. Trümper, 483

Kamphuis, J. 1993, Ph.D. thesis, Rijksuniversiteit Groningen

Kaneda, H., Makishima, K., Yamauchi, S., Koyama, K., Matsuzaki, K., & n. Y. Yamasaki. 1997, ApJ, 491, 638

Kenney, J. D. P., Scoville, N. Z., & Wilson, C. D. 1991, ApJ, 366, 432

Kenney, J. D. P., Wilson, C. D., Scoville, N. Z., Devereux, N. A., & Young, J. S. 1992, ApJ, L79

Kerr, F. J. 1993, in Back to the Galaxy, ed. S. S. Holt & F. Verter, 3

Kregel, M., van der Kruit, P. C., & de Grijs, R. 2002, MNRAS, 334, 646

Kuntz, K. D., & Snowden, S. L. 2000, ApJ, 543, 195

Kuntz, K. D., & Snowden, S. L. 2001, ApJ, 554, 684

Liedahl, D. A., Osterheld, A. L., & Goldstein, W. H. 1995, ApJ, 438, L115

Little, B., & Tremaine, S. 1987, ApJ, 320, 493

Lockman, F. J., & Gehman, C. S. 1991, ApJ, 382, 182

21

Markevitch, M. 2001, http://cxc.harvard.edu/-contrib/maxim/bg/index.html

Matonick, D. M., & Fesen, R. A. 1997, ApJS, 112, 49

McCammon, D., & Sanders, W. T. 1984, ApJ, 287, 167

Mewe, R., Gronenschild, E., & van den Oord, G. H. J. 1985, A&AS, 62, 197

Mewe, R., Lemen, J. R., & van den Oord, G. H. J. 1986, A&AS, 65, 511

Moody, J. W., Roming, P. W. A., Joner, M. D., Hintz, E. G., Geisler, D., Durrell, P. R., Scoween, P. A., & Jee, R. O. 1995, AJ, 110, 2088

Mukai, K., Snowden, S. L., Pence, W. D., & Kuntz, K. D. 2002, ApJ

Mushotzky, R. F., Cowie, L. L., Barger, A. J., & Arnaud, K. A. 2000, Nature, 404, 459

Okamura, S., Kanazawa, T., & Kodaira, K. 1976, PASJ, 28, 329

Pence, W. D., Snowden, S. L., Mukai, K., & Kuntz, K. D. 2001, ApJ, 561, 189

Pietz, J., Kerp, J., Kalberla, P., Burton, W. B., Hartmann, D., & Mebold, U. 1998, A&A, 332, 55

Rand, R. J. 1998, Proc. Astron. Soc. Aust., 15, 106

Raymond, J. C., & Smith, B. W. 1977, ApJS, 35

Shelton, R. L. 1999, ApJ, 521, 217

Smith, R. K. 2002, private communication

Smith, R. K., Brickhouse, N. S., Liedahl, D. A., & Raymond, J. C. 2001, ApJ, 556, L91

Snowden, S. L. 2001, The Century of Space Science, ed. J. Bleeker, J. Geiss, & M. Huber (Kluwer), Ch. The ISM, The Hot Part

Snowden, S. L., Egger, R., Finkbeiner, D., Freyberg, M. J., & Plucinsky, P. P. 1998, ApJ, 493, 715

Snowden, S. L., et al. 1997, ApJ, 485, 125

Snowden, S. L., Freyberg, M. J., Kuntz, K. D., & Sanders, W. T. 2000, ApJS, 128, 171

Snowden, S. L., Mukai, K., Pence, W., & Kuntz, K. D. 2001, AJ, 121, 3001

Snowden, S. L., & Pietsch, W. 1995, ApJ, 452, 627

Sodroski, T. J., Odegard, N., Arendt, R. G., Dwek, E., Weiland, J. L., Hauser, M. G., & Kelsall, T. 1997, ApJ, 480, 173

Spitzer, L. 1956, ApJ, 124, 20

Stecher, T. P., et al. 1997, PASP, 109, 584

Stetson, P. B., et al. 1998, ApJ, 508, 491

Timmes, F. X., Woosley, S. E., & Weaver, T. A. 1995, ApJS, 98, 617

Toft, S., Rasmussen, J., Sommer-Larsen, J., & Pedersen, K. 2001, MNRAS, 0, 0

Torres-Piembert, S., Piembert, M., & Fierro, J. 1989, ApJ, 345, 186

Trinchieri, G., Fabbiano, G., & Romaine, S. 1990, ApJ, 356, 110

Tully, R. B. 1988, Nearby Galaxies Catalogue (Cambridge University Press)

van der Kruit, P. C. 1988, A&A, 192, 117

van der Kruit, P. C. 1990, The Milky Way as a Galaxy, ed. R. Buser & I. King (University Science Books), Ch. Photometric Components in Disk Galaxies, 77

van der Kruit, P. C., & Searle, L. 1982, A&A, 110, 79

Wang, Q. D. 1998, in The Local Bubble and Beyond, ed. D. Breitschwerdt & M. Freyberg, 503

Wang, Q. D. 1999, ApJ, 510, L139

Wang, Q. D., Immler, S., & Pietsch, W. 1999, ApJ, 523, 121

Williams, R. M., & Chu, Y.-H. 1995, ApJ, 439, 132

Zaritsky, D., Elston, R., & Hill, J. M. 1990, AJ, 99, 1108